International Journal of Solids and Structures 45 (2008) 5088–5102

Contents lists available at ScienceDirect

International Journal of Solids and Structures

journal homepage: www.elsevier.com/locate/ijsolstr

Dispersion of elastic guided waves in piezoelectric infinite plates with inversion layers

Daniel H. Cortes [a], Subhendu K. Datta [b], Osama M. Mukdadi [a,c,*]

[a] Department of Mechanical and Aerospace Engineering, West Virginia University, P.O. Box 6106, Morgantown, WV 26506, United States
[b] Department of Mechanical Engineering, University of Colorado, CO 80309-0427, United States
[c] Center for Interdisciplinary Research in Cardiovascular Sciences, West Virginia University, Morgantown, WV 26506, United States

ARTICLE INFO

Article history:
Received 26 June 2007
Received in revised form 12 November 2007
Available online 24 May 2008

Keywords:
Piezoelectric material
Ultrasound transducers
Infinite plates
Guided waves
Harmonic imaging

ABSTRACT

In this work, we study the dispersion of elastic waves in piezoelectric infinite plates with ferroelectric inversion layers. The motivation is to analyze the effect of ferroelectric inversion layers on wave dispersion and resonant behavior under impulsive line loads. A semi-analytical finite-element (SAFE) method has been adopted to analyze the problem. Two model problems are considered for analysis. In one, the plate is composed of a layer of 36° rotated *y*-cut $LiNbO_3$ with a ferroelectric inversion layer. In the other, material is PZT-4 with a ferroelectric inversion layer. Comparison with experimental results, reported in the literature for isotropic materials, shows a very good agreement with theoretical predictions obtained using SAFE method. Furthermore, comparison of the resonance frequencies of the S_1 modes, calculated using KLM approximation ($f_0 = C_d/2h$) and SAFE method, are illustrated for each problem. The frequency spectra of the surface displacements show that resonant peaks occur at frequencies where the group velocity vanishes and the phase velocity remains finite, *i.e.*, a minimum in the dispersion curve below the cut-off frequency. The effect of the ratio of the thicknesses of the inversion layer (IL) and the plate on the frequencies and strength of the resonant peaks is examined. It is observed that for PZT-4 with 50% IL to plate thickness ratio the frequency for the second resonant peak is about twice that for the first one. Results are presented showing the dependence of resonant frequencies on the material properties and anisotropy. Materials selection for single-element harmonic ultrasound transducers is a very important factor for optimum design of transducers with multiple thickness-mode resonant frequencies. The theoretical analysis presented in this study should provide a means for optimum ultrasound transducer design for harmonic imaging in medical applications.

1. Introduction

Infinite plates have been widely used as a model for single element ultrasound transducers. Current ultrasound transducer design is based on exciting the resonant frequency of the first extensional mode (S_1) only. Thus, most manufacturers use equivalent approximate networks such as KLM, Mason and Redwood circuit models to design ultrasound transducers that are limited to the first resonant frequency of the extensional mode (S_1). For medical applications such as harmonic

* Corresponding author. Address: Department of Mechanical and Aerospace Engineering, West Virginia University, P.O. Box 6106, Morgantown, WV 26506, United States. Tel.: +1 304 293 3111x2380; fax: +1 304 293 8823.
E-mail address: sam.mukdadi@mail.wvu.edu (O.M. Mukdadi).
URL: http://www.mae.cemr.wvu.edu/ (O.M. Mukdadi).

0020-7683/$ - see front matter © 2008 Elsevier Ltd. All rights reserved.
doi:10.1016/j.ijsolstr.2008.05.010

imaging, it would be desirable to have a transducer operating with multiple resonant frequencies near the frequencies of interest (Wang and Chan, 2003; Frijlink et al., 2005, 2006; Bouakaz et al., 2002).

Finite-element methods (FEM) have been widely used to analyze piezoelectric structures. A full review of these is beyond the scope of this paper. Mention is made here of Saravanos and Heyliger (1995), Saravanos et al. (1997), Ramirez et al. (2006), and references therein. FEM has also been used to model ultrasound transducers (Lerch, 1990; Hossack and Hayward, 1991; McKeighen, 2001; Zhou et al., 2006). Time-domain schemes have been used to predict the performance of ultrasound transducers in terms of impedances and efficiencies. The effect of matching layers, backing layers, bonding layer and electrodes on the operation of the transducer can be addressed using this technique (Zhou et al., 2006; McKeighen, 2001). However, a large number of elements and simulation time are usually required for high frequency simulations. On the other hand, semi-analytical finite-element (SAFE) methods, where the discretization is used only in the thickness direction in an infinite plate (or the radial direction in a circular cylinder), have been used by Bai et al. (2004), Dong and Pauley (1978), Pauley and Dong (1974), Siao et al. (1994) and Taciroglu et al. (2004) for analysis of dispersion of guided waves and dynamic response. These are generalizations of the ones used for the analysis of guided waves in composite plates and circular cylinders (see the review by Datta, 2000). Mukdadi et al. (2002) and Mukdadi and Datta (2003) studied time-harmonic and transient guided waves in cylinders of rectangular cross section using the SAFE method.

Multilayered piezoelectric ceramics have been demonstrated to improve the performance of medical ultrasound transducers (Mills and Smith, 2002a,b; Goldberg and Smith, 1994). Mills and Smith (2002a) showed that the signal-to-noise ratio (SNR) increased by 11 dB and the bandwidth was improved by 40% when using three-layer PZT crystals for 2-D arrays. Goldberg and Smith (1994) found similar results for 1.5-D transducers made of a layered ceramic. Layers of different materials were also analyzed numerically by Mills and Smith (2002b) showing improvements on the bandwidth and SNR.

A recent improvement on the design of broadband ultrasound transducer by the introduction of an inversion layer (IL) has been reported (Nakamura et al., 2003, 2005; Zhou et al., 2006, 2005; Huang et al., 2005). The active element in an IL transducer is composed of two piezoelectric sublayers of opposite poling directions. In the ferroelectric inversion layer, the piezoelectric constants are opposite in sign to those of a regular one. Note that the equations governing wave motion in such an IL are the same as those in a regular one except for the change in sign of the piezoelectric constants. It has been demonstrated that the use of a layer of $LiNbO_3$ of 30% of the total thickness with inverted piezoelectric properties decreases the conversion loss at the second-order thickness-mode, *i.e.*, at a frequency equal to twice the fundamental resonance frequency. Zhou et al. (2005, 2006) used time-domain finite elements to study electrical impedance and acoustic characteristics of IL transducers.

In this paper, attention is focused on analyzing the effect of those lower-order propagating modes that have zero-group velocity (ZGV) points in the frequency–wavenumber domain. Although special properties of these points have been well known since the early studies of dispersion of guided waves in plates and cylinders, they have been exploited only recently for material characterization and dynamic response studies. Recent experimental studies (Clorennec et al., 2007; Gibson and Popovics, 2005; Holland and Chimenti, 2004; Veidt et al., 2000) have shown that strong resonances occur in plates at frequencies where the group velocities of S_1 and A_2 modes vanish, but the phase velocities have finite values, *i.e.*, the dispersion curves for those modes have minima below the cut-off frequencies. Since the group velocity of such a mode vanishes at the minimum, mechanical energy is trapped and high amplitude standing waves (vibrations) are present. The frequencies of the zero-group velocity (ZGV) points depend on the materials properties and the thickness of the plate. The frequency spectrum of the forced displacement response due to a frequency-dependent excitation shows the resonant peaks, from which the frequencies of the ZGV points can be obtained. Excitation of plates at frequencies in the neighborhood of ZGV points can be used to calculate the thickness or the Poisson's ratio for isotropic plates (Clorennec et al., 2007) or for imaging of flaws (Holland and Chimenti, 2004).

The same concept has been used to refine another NDT method called 'Impact Test' (Gibson and Popovics, 2005) or traditional transducer excitation for nondestructive evaluation of composite plates (Veidt et al., 2000). In these, the normal displacements of a plate structure are measured after an impact or a force is applied to the structure. The frequency spectra of these displacements are used to detect the resonant frequencies and then material properties or thickness can be calculated.

In this paper, we have used the SAFE method to analyze the dispersion behavior and the forced response of a piezoelectric plate with an inversion layer with particular attention to frequencies near ZGV points. $LiNbO_3$ and PZT-4 plates, with various percentages of inversion layers have been analyzed to explore the relation between ZGV points and resonant peaks in the frequency spectra of the displacement and the effect of IL on the first two resonant frequencies. Corresponding modes shapes at the ZGV regions are also discussed. This analysis provides a better understanding of the IL effect and may be used as analytical tool to optimize the design of broadband ultrasound transducers.

2. Finite-element formulation

2.1. Governing equations

Consider a layered piezoelectric plate as shown in Fig. 1. The piezoelectric plate consists of N parallel, homogeneous, and anisotropic layers, which are perfectly bonded together. A global rectangular coordinate system (X,Y,Z) is adopted such that the Z-axis coincides with the thickness direction. The X and Y axes are parallel to the infinite direction of the plate. We adopt a hybrid analytical–numerical approach to model elastic guided wave propagation in layered anisotropic infinite piezoelectric plates. The analysis couples analytical treatment of the motion in the XY plane with a numerical treatment of the motion

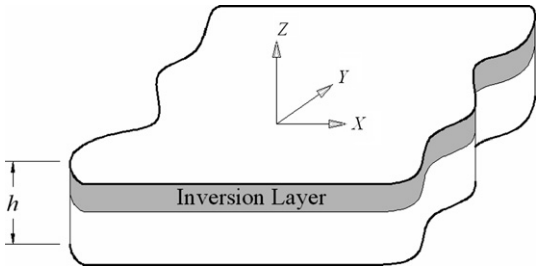

Fig. 1. Coordinate system and inversion layer distribution.

along the thickness direction of the plate using the finite-element method. To effect the latter, we discretize the thickness (Z-axis) of the plate using three-node finite-elements, each of which has associated with it a local coordinate system (x,y,z), which is parallel to the global coordinate system. The displacement and electric potential are assumed to be time-dependent and functions of local coordinates system (x,y,z). Since the displacements are small compared to the thickness, a linear stress–strain-electrical field will be used to describe the dynamic behavior of the plate. The constitutive equation in the matrix form is given by

$$\mathbf{Q} = \mathbf{C}^{*}\mathbf{q}, \tag{1}$$

where $\mathbf{Q} = [T_{xx}, T_{yy}, T_{zz}, T_{yz}, T_{xz}, T_{xy}, D_x, D_y, D_z]$ is a vector of the stress components and the electric displacements, $\mathbf{q} = [S_{xx}, S_{yy}, S_{zz}, 2S_{yz}, 2S_{xz}, 2S_{xy}, E_x, E_y, E_z]$ is a vector with the components of the mechanical strain and electric field components, and $\mathbf{C}^{*}$ is a matrix containing the elastic constants $\mathbf{c}$, dielectric constants $\boldsymbol{\varepsilon}$ and the piezoelectric stress constants $\mathbf{e}$:

$$\mathbf{C}^{*} = \begin{bmatrix} \mathbf{c} & -\mathbf{e}^{\mathrm{T}} \\ \mathbf{e} & \boldsymbol{\varepsilon} \end{bmatrix}. \tag{2}$$

Without loss of generality, we assume that the waves are propagating in the x-direction. The kinematic equation relates the vector $\mathbf{q}$ to the displacements and electric potential vector $\mathbf{v} = [u_x, u_y, u_z, \phi]$ as,

$$\mathbf{q} = \mathbf{B}_1\mathbf{v}^{e}_{,x} + \mathbf{B}_2\mathbf{v}^{e}, \tag{3}$$

where $\mathbf{B}_1$ and $\mathbf{B}_2$ are operator matrices defined in Appendix A.

The equation of motion can be obtained using the Hamilton's principle (Tiersten, 1969):

$$\delta \int_{t_0}^{t_1} (\mathrm{KE} - H + W)\mathrm{d}t = 0, \tag{4}$$

where KE, H and W are the kinetic energy, electrical enthalpy and potential energy of the prescribed surface forces and charges, respectively. These terms can be expressed as:

$$\mathrm{KE} = \frac{1}{2}\int\int\int_{\upsilon} \dot{\mathbf{v}}^{\mathrm{T}}\boldsymbol{\rho}\dot{\mathbf{v}}\,\mathrm{d}\upsilon, \quad H = \frac{1}{2}\int\int\int_{\upsilon} \mathbf{q}^{\mathrm{T}}\mathbf{C}\mathbf{q}\,\mathrm{d}\upsilon, \quad \text{and } W = \int\int_{S} \mathbf{v}^{T}\mathbf{f}\,\mathrm{d}S, \tag{5}$$

where, $\mathbf{C} = \begin{bmatrix} \mathbf{c} & -\mathbf{e}^{\mathrm{T}} \\ -\mathbf{e} & -\boldsymbol{\varepsilon} \end{bmatrix}$, and $\boldsymbol{\rho} = \begin{bmatrix} \rho & & & \\ & \rho & & \\ & & \rho & \\ & & & 0 \end{bmatrix}$.

The thickness direction of the plate is discretized using three-node elements. Within each sublayer, quadratic interpolation functions with three equally spaced nodal surfaces are used. The explicit form of these interpolations over a sublayer is shown in Appendix A.

The field variables $\mathbf{v}$ can be written in terms of the vector of nodal variables $\mathbf{v}^{e}$ as follows:

$$\mathbf{v}(x,z,t) = \mathbf{N}(z)\mathbf{v}^{e}(x,t), \tag{6}$$

where $\mathbf{N}$ is a matrix composed of the interpolation functions. The equations of motion are obtained by substitution of Eq. (6) into Eq. (5) and carrying out the variation of Eq. (4), analogous to that used by Mukdadi et al. (2002) and Mukdadi and Datta (2003) (details are shown in Appendix A):

$$\mathbf{m}^{e}\ddot{\mathbf{v}}^{e} + \mathbf{k}^{e}_{1}\mathbf{v}^{e} + \mathbf{k}^{e}_{2}\mathbf{v}^{e}_{,x} - \mathbf{k}^{e}_{3}\mathbf{v}^{e}_{,xx} = \mathbf{f}^{e}. \tag{7}$$

Eq. (7) is a system of partial differential equations that relates the electromechanical response due to mechanical and/or electrical excitation. Global mass and stiffness matrices can be obtained considering the connectivity of the discretized geometry. Eq. (7) can be expressed in its global form as:

$$\mathbf{M}\ddot{\mathbf{V}} + \mathbf{K}_1\mathbf{V} + \mathbf{K}_2\mathbf{V}_{,X} - \mathbf{K}_3\mathbf{V}_{,XX} = \mathbf{F}, \tag{8}$$

where,

$$\mathbf{M} = \cup \mathbf{m}^e, \quad \mathbf{K}_i = \cup \mathbf{k}_i^e, \quad \mathbf{F} = \cup \mathbf{f}^e, \quad \text{and} \quad \mathbf{V} = \cup \mathbf{v}^e.$$

A comma (,) represents the spatial first derivative with respect to the global coordinates. To solve Eq. (8), a semi-analytical technique will be implemented in the following section. In this study, we consider open circuit ($D_Z = 0$) and traction-free ($T_{XZ} = T_{ZZ} = 0$) boundary conditions on the upper and lower surfaces of the plate. Note that Eq. (8) is the semi-analytical finite-element equation, which is obtained by discretizing in the Z-direction. This equation can now be solved by using standard Fourier transforms techniques in X and t.

Define the Fourier transformation as

$$\widetilde{\Phi}(k,\omega) = \int_{-\infty}^{\infty}\int_{-\infty}^{\infty} \Phi(X,t) \mathrm{e}^{-\mathrm{i}(kX-\omega t)}\, \mathrm{d}X\, \mathrm{d}t, \tag{9}$$

where $\Phi(X,t)$ is a finite function, k and ω represent the wave numbers along X direction and the angular frequency, respectively. Applying this transformation to Eq. (8), the differential equation is transformed into:

$$(\mathbf{K}_1 - \mathrm{i}k\mathbf{K}_2 + k^2\mathbf{K}_3 - \omega^2\mathbf{M})\widetilde{\mathbf{V}} = \widetilde{\mathbf{F}}. \tag{10}$$

The dispersion relations of the propagating modes are found by solving the eigenvalue problem arises when considering the homogeneous case ($\widetilde{\mathbf{F}} = \mathbf{0}$) of Eq. (10). If the wavenumber k is defined, then Eq. (10) can be solved for the angular frequencies ω of the propagating modes. The phase and group velocities can be expressed, respectively, as,

$$v_p = \frac{\omega}{k}, \quad \text{and} \quad v_g = \frac{\partial \omega}{\partial k}. \tag{11}$$

Dispersion curves showing the dependence of the phase and group velocities on the angular frequencies can be obtained using Eqs. (10) and (11).

2.2. Electro-elastodynamic Green's functions

Solving the homogenous part of Eq. (10) will yield the dispersion relation for elastic guided waves in infinite piezoelectric plates. To derive the Green's functions, one can rewrite Eq. (10) including the forcing term in the form (Mukdadi and Datta, 2003),

$$[\mathbf{A}]\mathbf{U} = \gamma[\mathbf{B}]\mathbf{U} + \mathbf{P}, \tag{12}$$

where

$$\mathbf{A} = \begin{bmatrix} \mathbf{0} & \mathbf{I} \\ \mathbf{K}_1 - \omega^2\mathbf{M} & -\mathbf{K}_2 \end{bmatrix}, \quad \mathbf{B} = \begin{bmatrix} \mathbf{I} & \mathbf{0} \\ \mathbf{0} & \mathbf{K}_3 \end{bmatrix},$$

and

$$\mathbf{U} = [\,\widetilde{\mathbf{V}} \quad \gamma\widetilde{\mathbf{V}}\,]^T, \ \mathbf{P} = [\,\mathbf{0} \quad \widetilde{\mathbf{F}}\,]^{\mathrm{T}}, \ \text{and} \quad \gamma = \mathrm{i}k.$$

Note that matrix $\mathbf{A}$ is not symmetric but $\mathbf{B}$ is symmetric. The homogenous part of Eq. (12) will yield the characteristic equation, the roots of which (eigenvalues) are the wavenumbers of the modes for a given frequency ω. These wavenumbers can be real, imaginary or complex numbers. The imaginary and complex eigenvalues correspond to the evanescent modes, while real values are for the propagating modes.

The right and left eigenvectors, φ_m and ψ_m, respectively, associated with each eigenvalue can be found solving the systems of equations (written in an abbreviated form)

$$[\mathbf{A} - \gamma_m\mathbf{B}]\varphi_m = \mathbf{0}, \quad \text{and} \quad [\mathbf{A}^{\mathrm{T}} - \gamma_m\mathbf{B}]\psi_m = \mathbf{0}. \tag{13}$$

Here, φ_m and ψ_m satisfy the bi-orthogonality relations:

$$\psi_m^{\mathrm{T}}\mathbf{B}\varphi_m = \delta_{mn}B_n, \quad \text{and} \quad \psi_m^{\mathrm{T}}\mathbf{A}\varphi_m = \delta_{mn}\gamma_m B_n. \tag{14}$$

The eigenvectors can be combined as the upper and lower parts to give

$$\varphi_m = \begin{Bmatrix} \varphi_{mu} \\ \varphi_{ml} \end{Bmatrix} = \begin{Bmatrix} \varphi_{mu} \\ \gamma_m\varphi_{ml} \end{Bmatrix}, \quad \psi_m = \begin{Bmatrix} \psi_{mu} \\ \psi_{ml} \end{Bmatrix} = \begin{Bmatrix} \psi_{mu} \\ \gamma_m\psi_{ml} \end{Bmatrix}. \tag{15}$$

These eigenvectors can be used to calculate the response spectrum due to electrical or mechanical excitations. The solution of Eq. (12) is the weighted sum of all modes:

$$\mathbf{U}(\gamma,\omega) = \sum_{m=1}^{2N} \overline{U}_m\varphi_m. \tag{16}$$

Inserting Eq. (16) into Eq. (12), the following system of equations is obtained:

$$[\mathbf{A} - \gamma \mathbf{B}] \sum_{m=1}^{2N} \overline{U}_m \varphi_m = \mathbf{P}. \tag{17}$$

Multiplying Eq. (17) on the left side by ψ_m^{T} and applying the bi-orthogonality relations, the $\overline{U}_m$ coefficients can be obtained:

$$\overline{U}_m = \frac{\psi_m^{\mathrm{T}} \mathbf{P}}{(\gamma_m - \gamma) B_m}. \tag{18}$$

In terms of the lower and upper eigenvectors (Eq. (15)), we expressed the resulting Green's functions in the wavenumber–frequency domain by substituting $\overline{U}_m$ in Eq. (16) as follows,

$$\widetilde{\mathbf{V}}(\gamma, \omega) = \sum_{m=1}^{2N} \frac{\gamma_m \psi_{mu}^{\mathrm{T}} \widetilde{\mathbf{F}}}{(\gamma_m - \gamma) B_m} \varphi_{mu}. \tag{19}$$

Table 1a
Mechanical properties and mass densities of steel, 36° rotated *y*-cut $LiNbO_3$ and PZT-4 materials (Zhou et al., 2006; Auld, 1990)

	Elastic properties (GPa)							Density (kg/m^3)
	C_{11}	C_{12}	C_{13}	C_{14}	C_{33}	C_{44}	C_{66}	ρ
Steel	277.5	113.4	113.4	0	277.5	82	82	7850
36° rotated *y*-cut $LiNbO_3$	199	51.85	70.85	3.91	203.96	70.75	60.44	4640
PZT-4	139	77.8	74.3	0	115	25.6	30.6	7500

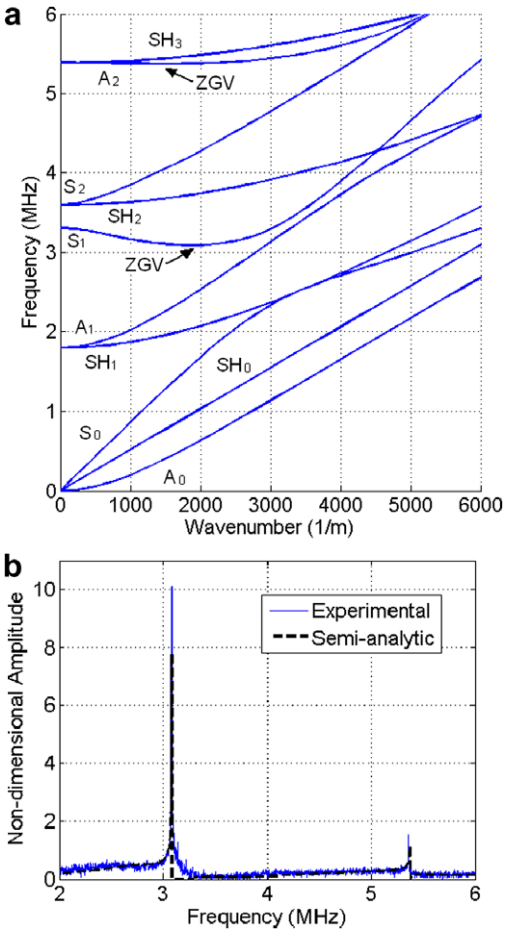

Fig. 2. Vibrational characteristics of a steel plate of 0.9 mm thick: (a) dispersion curves, (b) frequency spectra of the normal displacement.

The displacement and electrical potential in the space–frequency domain were determined by applying the inverse Fourier transform, which was evaluated numerically using Cauchy's residue theorem,

$$\widehat{\mathbf{V}}(X;\omega) = -\mathrm{i}\sum_{m=1}^{N} \frac{\gamma_m \psi_{mu}^T \widetilde{\mathbf{F}}}{B_m} \varphi_{mu} \mathrm{e}^{-\gamma_m X}. \tag{20}$$

Eq. (20) represents the displacement and electrical potential Green's functions in the space–frequency domain due to force or electric excitation.

2.3. Frequency response due to impulse loading

To obtain ultrasound images with optimum axial and lateral spatial resolutions, impulsive loads are usually used with broadband ultrasound transducers. In this study, we aim to study the resonance modes of elastic guided waves for harmonic

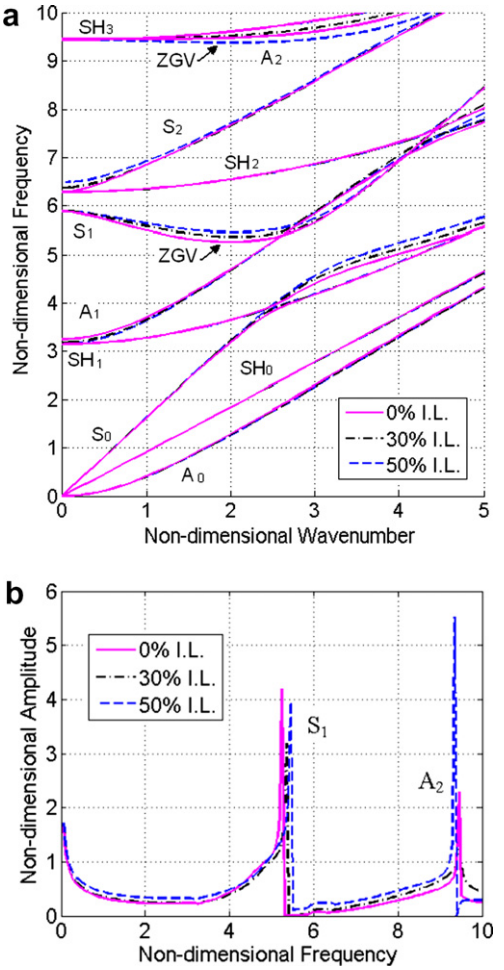

Fig. 3. Vibrational behavior of 36° rotated *y*-cut $LiNbO_3$ plate for several percentages of inversion layer and 0.5 mm thickness: (a) dispersion curves, (b) frequency spectra of the normal displacement.

Table 1b
Piezoelectric properties of 36° rotated *y*-cut $LiNbO_3$ and PZT-4 materials (Zhou et al., 2006; Auld, 1990)

	Piezoelectric stress constant (C/m^2)			Clamped dielectric constants	
	e_{15}	e_{31}	e_{33}	ε_{33}	ε_{11}
36° rotated *y*-cut $LiNbO_3$	1.544	−1.152	3.628	32.99	44.9
PZT-4	12.7	−5.2	15.1	635	730

ultrasound transducer design. To do so, we considered an impulsive line load applied to the surface of the piezoelectric plate. This line load along the *Y*-axis is acting into the thickness direction of the plate (*Z*-axis). This impulse line load can be expressed in the form,

$$\mathbf{F}(X,t) = \delta(X)\delta(t)\mathbf{F}_0, \tag{21}$$

where $\mathbf{F}_0$ is a vector with all the components equal to zero, except one component corresponding to force acting into *Z*-axis or charge applied on the piezoelectric plate. Applying the Fourier transform (Eq. (9)) to Eq. (21) results in

$$\widetilde{\mathbf{F}}(k_X, k_Y, \omega) = \mathbf{F}_0. \tag{22}$$

The frequency spectrum of the normal displacements and electrical potential can be expressed, using Eq. (20), as:

$$\widehat{\mathbf{V}}(X;\omega) = -\mathrm{i}\sum_{m=1}^{N} \frac{\gamma_m \psi_{mu}^T \mathbf{F}_0}{B_m} \varphi_{mu} \mathrm{e}^{-\gamma_m X}. \tag{23}$$

The above equation represents the frequency response of the displacement and electrical potential at the point *X* due to a line force along the *Y*-axis and acting in the *Z*-direction. The numerical results illustrated in the following section will consider the frequency spectrum of the normal displacement calculated at the same point of excitation (*i.e.*, $X = 0$). This is analogous to the experiment reported by Clorennec et al. (2007).

3. Numerical results and discussion

Eqs. (10) and (23) govern the dispersion behavior and the frequency spectrum of displacements and electrical potential of guided wave propagation in layered piezoelectric infinite plates. In this study, numerical results for single layer and bi-layered plates used for fabricating single-element medical ultrasound transducers will be addressed.

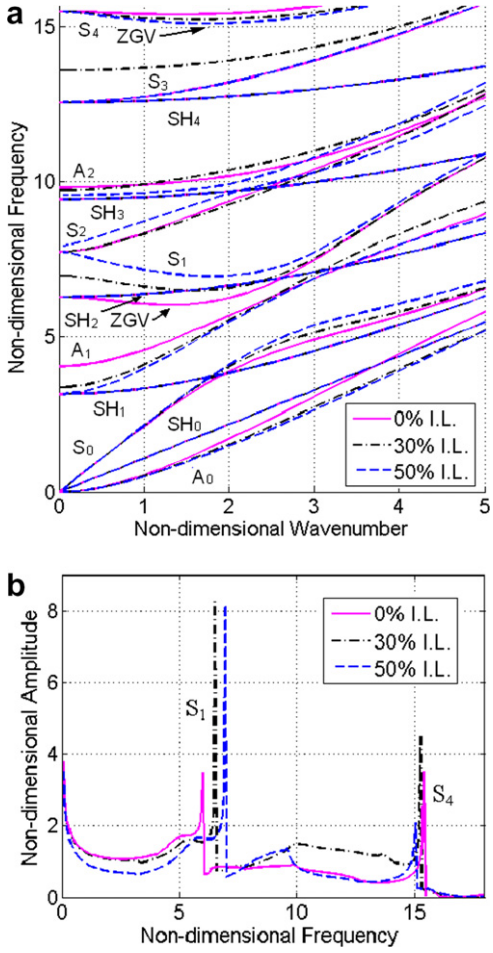

Fig. 4. Vibrational behavior of PZT-4 plate for several percentages of inversion layer and 0.5 mm thickness: (a) dispersion curves, (b) frequency spectra of the normal displacement.

Validation of the SAFE method with experiment was made by comparison of numerical results for a 0.9 mm steel plate and experimental results reported by Clorennec et al. (2007). The mechanical properties used for steel are shown in Table 1a. The dispersion curves for a steel plate of 0.9 mm show two ZGV points at 3.08 and 5.36 MHz (Fig. 2a), corresponding to the first extensional (S_1) and second flexural (A_2) modes. Excellent agreement for the peaks and off-peak values is observed between the frequency spectra of the normal displacement obtained by this method and experimental results (Fig. 2b). A comparison between the dispersion curves and the frequency spectra of the normal displacement clearly show that resonance peaks correspond to ZGV frequency points. This phenomenon shall be useful for piezoelectric resonators and ultrasound transducers used for imaging. Note that even though the experiment was for a point load, the frequency dependence of the displacement is the same for the point and line loads (except for a normalization factor). This is because the dispersion behavior is the same in two and three dimensions for an isotropic plate.

Table 2
Comparison of the resonance frequencies for several percentages of IL thickness ratios using SAFE method

	IL (%)	1st f_{SAFE} (ω/ω_0)	2nd f_{SAFE} (ω/ω_0)	2nd f_{SAFE}/1st f_{SAFE}
36° rotated *y*-cut $LiNbO_3$	0	5.25	9.45	1.78
	30	5.34	9.44	1.77
	50	5.46	9.35	1.71
PZT-4	0	6.00	15.40	2.57
	30	6.50	15.25	2.35
	50	6.95	15.05	2.16

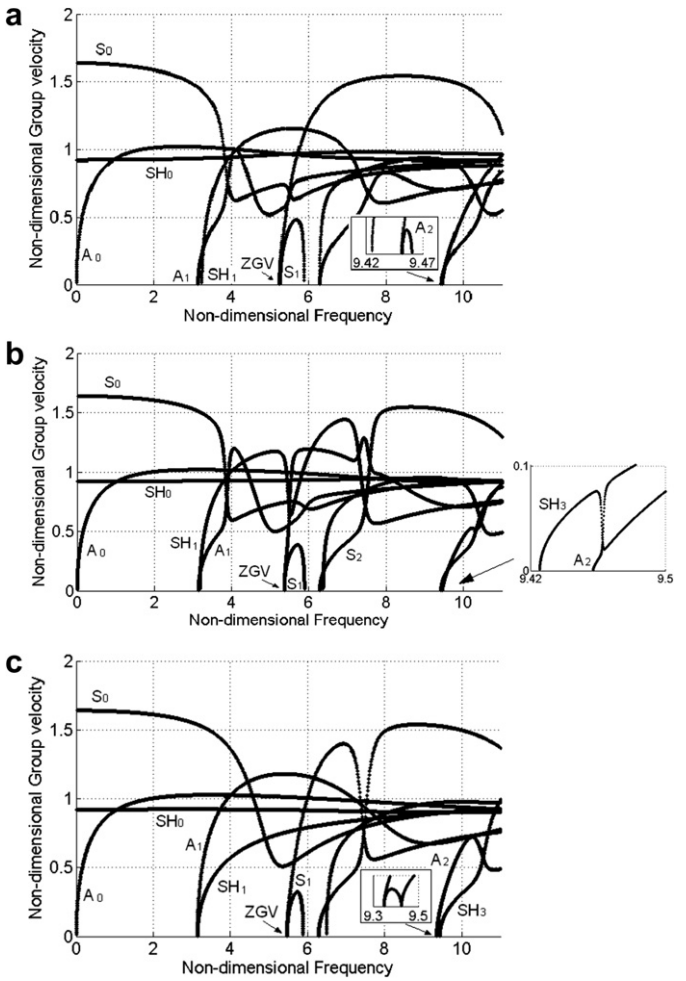

Fig. 5. Group velocity spectrum for 36° *y*-cut $LiNbO_3$: (a) 0% IL, (b) 30% IL, (c) 50% IL.

Fig. 3 shows the dispersion curves and the frequency spectra of the normal displacement of a 36° rotated *y*-cut $LiNbO_3$ layered plate of 0.5 mm total thickness. The effect of the ratio of the thickness of the inversion layer (IL) to the total thickness of the plate was examined. The mechanical and piezoelectric properties are shown in Table 1a and 1b, respectively. The wavenumber was normalized by multiplying with the thickness (h) and the non-dimensional frequency is defined as ω/ω_0 where by $\omega_0 = \sqrt{C_{44}/\rho}/h$. Here C_{44} is an elastic constant and ρ the mass density. The dispersion curves (Fig. 3a) for several ratios (0%, 30% and 50%) of IL thickness to the plate show negligible differences for shear-horizontal modes SH_0, SH_2 and SH_3. For the first-order shear-horizontal SH_1 mode, the curves are identical for k in the range 0–2.5, but after that, small differences are seen for the three percentages of IL thickness ratios. Small differences are observed for the S_0, S_1 and S_2 modes. The cut-off frequencies for the SH_1 and A_1 modes show small differences for 0% and 30% of IL, but are the same for 50% thickness ratio of IL. On the other hand, for SH_2 and S_2 modes, the cut-off frequencies are slightly different for 30% and 50% thickness ratios of IL. However, these cut-off frequencies for SH_2 and S_2 modes are equal for single $LiNbO_3$ plate without inversion layer (*i.e.*, 0% IL thickness ratio). The ZGV point for the S_1 mode does not change considerably. However, the lowest frequency for this ZGV point corresponds to 0% IL thickness ratio. On

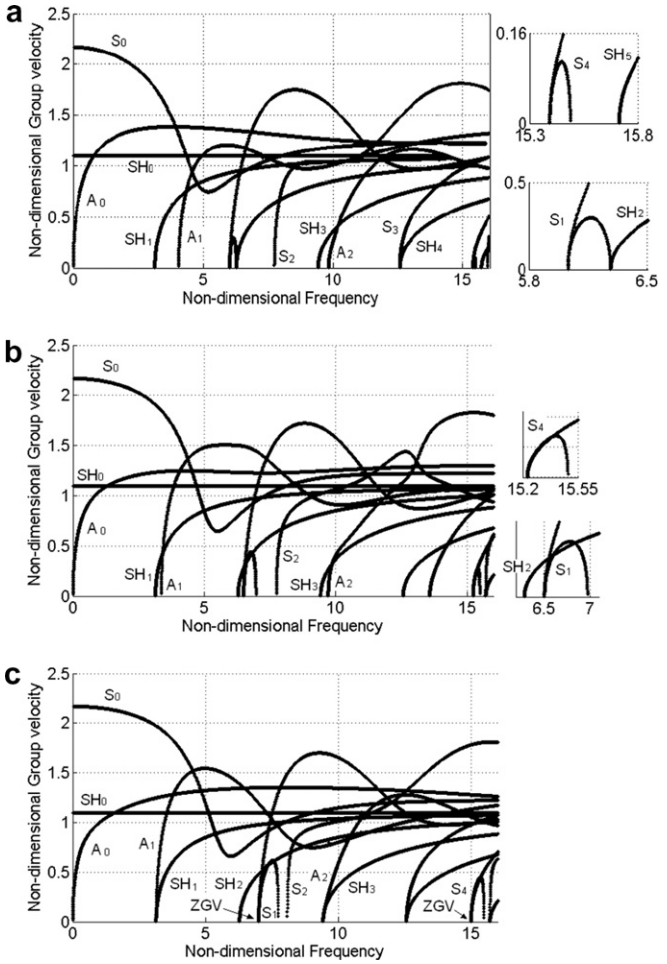

Fig. 6. Group velocity spectrum for PZT-4: (a) 0% IL, (b) 30% IL, (c) 50% IL.

Table 3
Comparison of the resonance frequencies calculated using the KLM approximation ($f_0 = C_d/2h$) and using SAFE method

	$f_0 = C_d/2h$ (MHz)	f_{SAFE} (MHz)	f_{SAFE}/f_0	$2f_0$ (MHz)	2nd f_{SAFE} (MHz)	2nd $f_{SAFE}/2f_0$
36° rotated *y*-cut $LiNbO_3$	7.10	6.57	0.92	14.20	11.75	0.827
PZT-4	3.92	3.52	0.90	7.82	9.05	1.156

the other hand, the lowest frequency for the ZGV point corresponding to the A_2 mode is obtained for 50% IL thickness ratio.

A similar analysis of the dispersion curves (Fig. 4a) for PZT-4 (Table 1) shows that the shear-horizontal SH_0, SH_1, SH_2 and SH_3 modes are similar for all the ratios of IL analyzed. A considerable difference is observed for the cut-off frequencies of the A_1 mode, especially for 0% IL thickness ratio. In a similar way, the cut-off frequencies for S_1 modes show considerable differences. It is noted that, the cut-off frequencies of S_1 and SH_2 modes are the same for 0% IL thickness ratio. The same is found to be true for the S_1 and S_2 for 50% of IL. A very important observation is that for this material the second ZGV point is not present on A_2 mode dispersion curve, but is found on that of S_4. Negishi (1987) showed that for isotropic materials a ZGV point for the A_2 mode exists only when the Poisson's ratio (v) is less than 0.31. Furthermore, ZGV points can be also found for S_3, S_4, S_6 and A_5 modes for specific values of v. In fact, there is not an explicit relation between the ZGV points and the elastic constants for anisotropic materials.

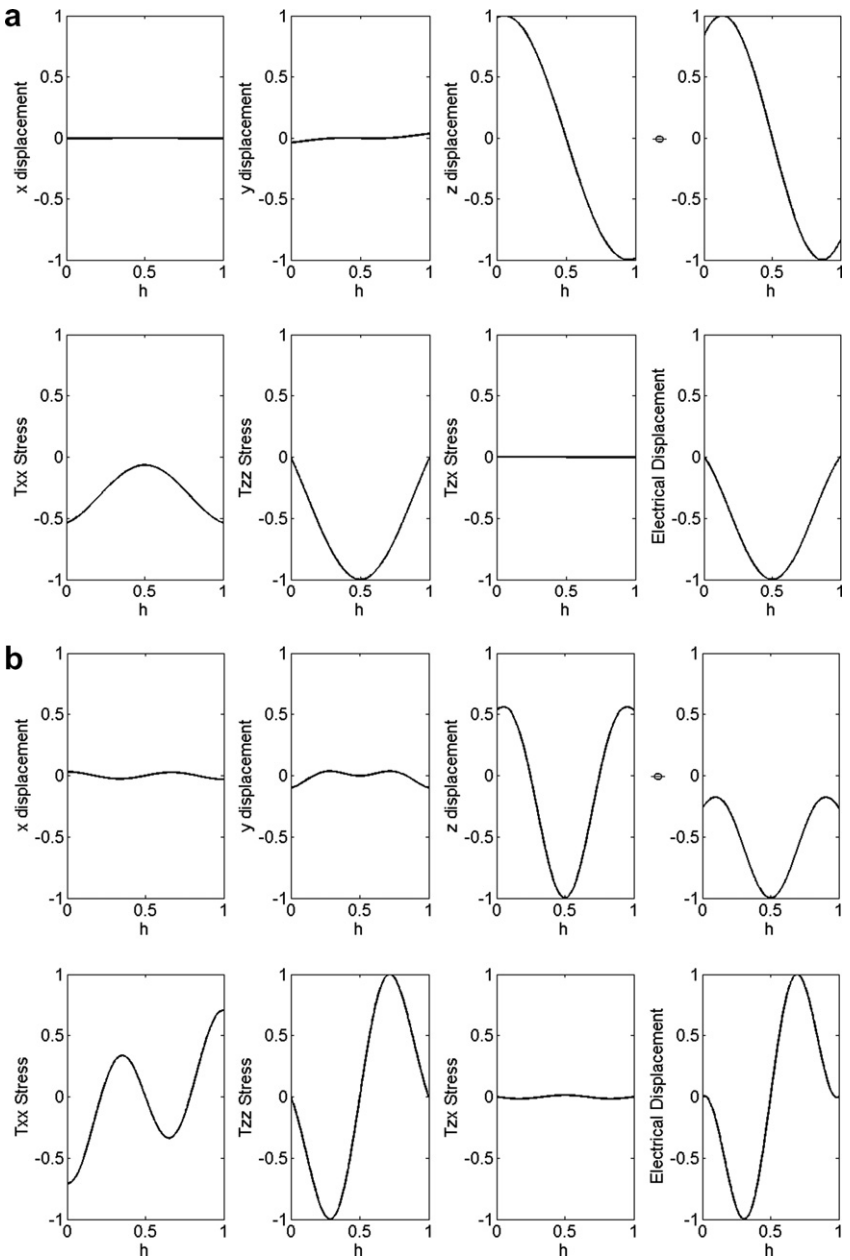

Fig. 7. Mode-shapes at resonant frequencies for 36° y-cut $LiNbO_3$ with 0% inversion layer: (a) S_1 mode, (b) A_2 mode.

Figs. 3b and 4b clearly show that the resonant frequencies for the plates correspond to the ZGV points on the dispersion curves. For $LiNbO_3$, the first two resonant peaks correspond to the ZGV of S_1 and A_2 modes. In the same way, for PZT-4, the first two resonant peaks are obtained for the ZGV points of S_1 and S_4 modes. The change in the frequency for the resonant peaks with the change in percentage of IL is small, except for first resonant peak for PZT-4. In this case, the resonant frequency was shifted from $\omega/\omega_0 = 6.0$ to $\omega/\omega_0 = 6.95$. Small peaks are observed at the cut-off frequency for the A_2 mode, especially for 50% IL thickness ratio. A comparison between the resonant frequencies obtained using the SAFE method presented here (Table 2) shows that the second resonant peak for PZT-4 with 50% IL thickness ratio is located at almost twice the frequency of the first peak, making this configuration optimum for harmonic imaging. Additionally, there is no significant difference in the ratio of the first two resonant frequencies of $LiNbO_3$ when the percentage of IL thickness ratio is changed.

Fig. 5 shows the frequency dependence of the non-dimensional group velocity $\left(\bar{v}_g = v_g/\sqrt{C_{44}/\rho}\right)$ for $LiNbO_3$. The group velocities were calculated using Eq. (11). It is clearly seen that for all percentages of inversion layer there is a ZGV point for the S_1 mode below the cut-off frequency. However, there is no ZGV point for the second anti-symmetric A_2 mode with 30% IL

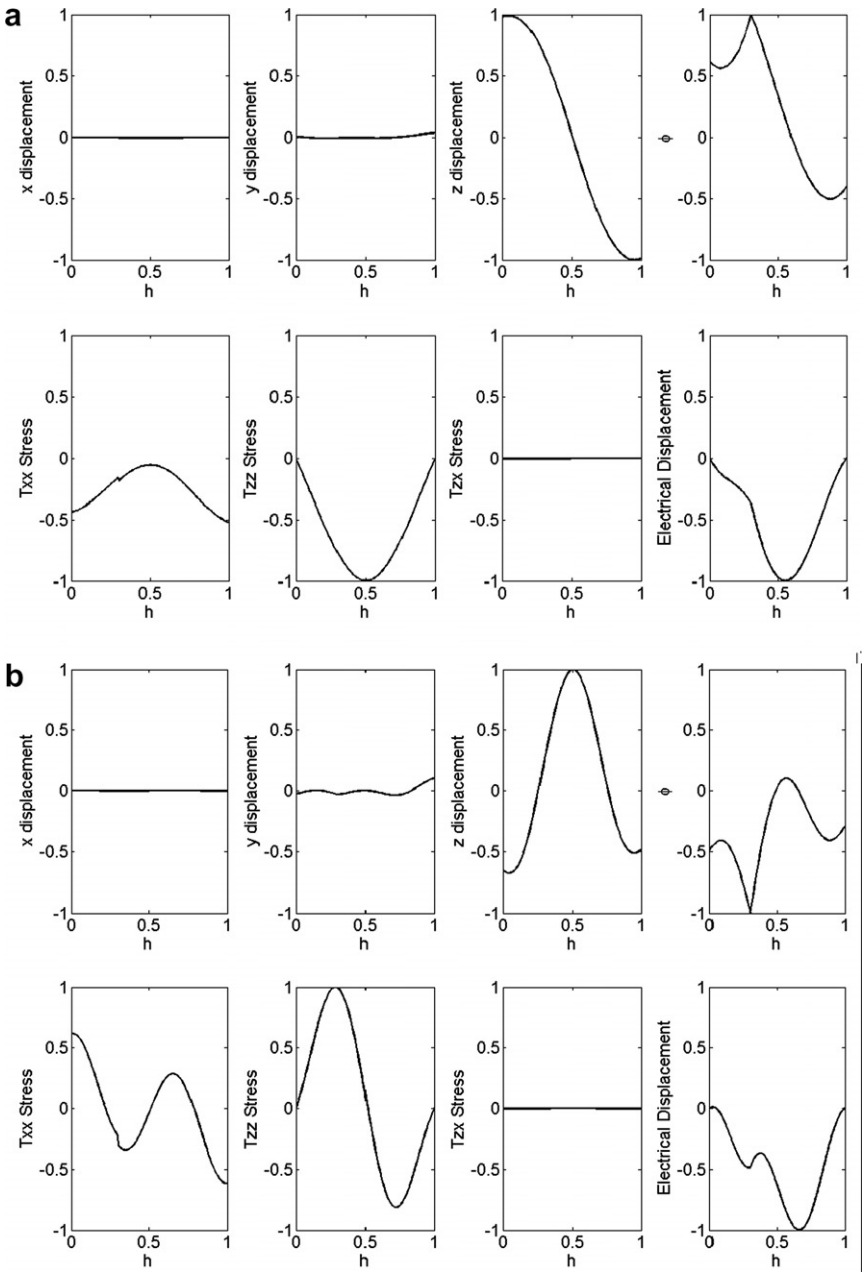

Fig. 8. Mode-shapes at resonant frequencies for 36° *y*-cut $LiNbO_3$ with 30% inversion layer: (a) S_1 mode, (b) A_2 mode.

thickness ratio, instead a crossing between the A_2 and SH_3 modes is observed. Fig. 6 shows the group velocity dispersion curves for PZT-4. The ZGV points for S_1 and S_4 modes are observed for all thickness ratios of IL. These results show strong influence of the piezoelectric material anisotropy on the ZGV modes, resonance characteristics and dispersion behavior of layered piezoelectric plates used for ultrasound imaging transducers. These theoretical findings provide a means for optimizing resonance characteristics of piezoelectric resonators.

In the approximate conventional methods (KLM) for transducer design the resonance frequency is defined as $f_0 = C_d/2h$, where $C_d = \sqrt{C_{33}/\rho}$ is the bulk dilatational speed of the piezoelectrical material and h the thickness. A comparison of the first and second resonance frequencies obtained using this method and the one proposed here for 0% IL thickness ratio is shown in Table 3. The error in calculating the first resonance for 36° rotated y-cut $LiNbO_3$ and PZT-4 is about 10%. For the second resonant frequencies the errors are considerably high for both materials (about 17%). These differences indicate that the resonant frequencies are strongly influenced by the material prop-

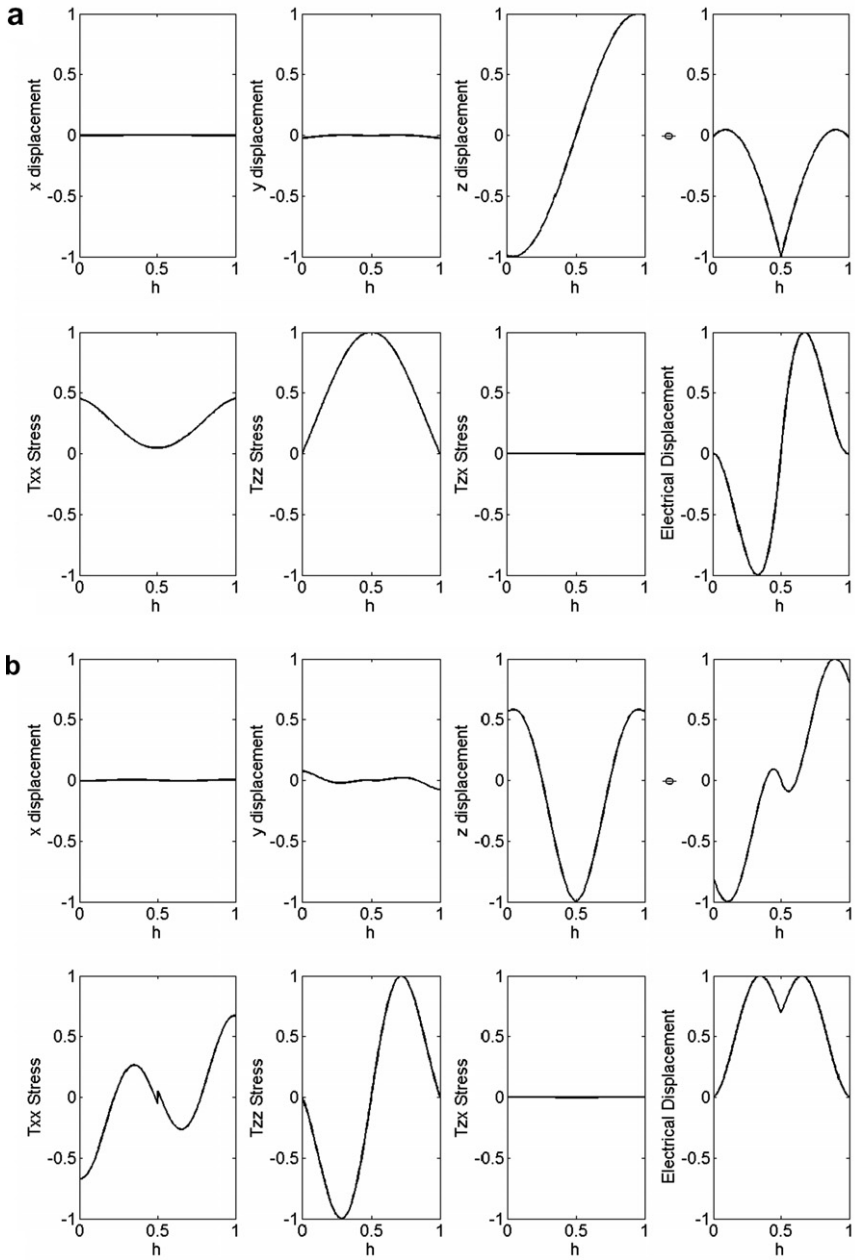

Fig. 9. Mode-shapes at resonant frequencies for 36° y-cut $LiNbO_3$ with 50% inversion layer: (a) S_1 mode, (b) A_2 mode.

erties and thus should be carefully obtained specially when designing multi-resonant transducers for harmonic imaging.

Recent studies have shown the improvement in the bandwidth for transducers made of $LiNbO_3$ when 30% IL thickness ratio has been included (Zhou et al., 2005, 2006; Nakamura et al., 2003, 2005). Zhou et al. (2006) showed that the bandwidth can be increased up to 90% using IL and a proper selection of the matching layers. Nakamura et al. (2003) found that the transducer characteristics depend on whether the IL is in the front (upper) or back (lower) sides of the transducer. However, in both cases the total efficiency of the transducer was improved at f_0 and $2f_0$.

The mode-shapes for the displacements, stresses and electrical displacements and voltage at the resonant frequencies are shown in Figs. 7–9. The displacements and stresses were normalized by the maximum overall value to preserve their relative magnitude. The electrical variables were normalized independently. It is clearly seen that the values of the stress components T_{ZZ}, T_{XZ} and electrical displacement D_Z are zero at the surfaces for all cases. Note that the free boundary conditions are the natural boundary conditions. Displacements in all coordinate directions are observed. However, there is a dominant displacement component and the others are very small. The mechanical displacements and stresses show no significant change with a change in the IL percentage. The electrical displacements and the stresses are observed to be divided into two regions corresponding to the inversion layer zones. Chen et al. (2007) also reported very small changes in the mechanical displacements of magneto-electro-elastic plates for changes in the piezoelectric and/or piezomagnetic properties.

4. Conclusions

A semi-analytical finite-element method has been used to theoretically predict the resonant frequencies and the dispersion behavior of layered piezoelectric plates. The analysis of piezoelectric layered plates shows that the resonant frequencies at the ZGV points of the Lamb wave modes are more significant than those at the cut-off frequencies. This is consistent with previous observations on Lamb waves in homogeneous and composite plates. It was also shown that the material properties as well as the percentage of inversion layer have measurable effect on the occurrence of the first and second resonance peak frequencies. A comparison between the resonant frequencies obtained by this method and analytical approximations, usually adopted for transducer design, showed considerable differences, especially for the second resonant frequency. The modal analysis showed that the mechanical displacements and stresses are independent of the changes in the thickness of the inversion layer. The theoretical analysis presented in this study provides a useful means for accurately calculating high-order resonance modes and ZGV points. It is believed that the method presented here would be useful for the design and optimization of ultrasound transducers for harmonic iimaging.

Appendix A. The matrices shown in Eq. (3) are defined as,

$$\mathbf{B_1} = \begin{bmatrix} \mathbf{N} & \cdot & \cdot & \cdot \\ \cdot & \cdot & \cdot & \cdot \\ \cdot & \cdot & \cdot & \cdot \\ \cdot & \cdot & \cdot & \cdot \\ \cdot & \cdot & \mathbf{N} & \cdot \\ \cdot & \mathbf{N} & \cdot & \cdot \\ \cdot & \cdot & \cdot & -\mathbf{N} \\ \cdot & \cdot & \cdot & \cdot \\ \cdot & \cdot & \cdot & \cdot \end{bmatrix}, \quad \text{and } \mathbf{B_2} = \begin{bmatrix} \cdot & \cdot & \cdot & \cdot \\ \cdot & \cdot & \cdot & \cdot \\ \cdot & \cdot & \mathbf{N}_{,z} & \cdot \\ \cdot & \mathbf{N}_{,z} & \cdot & \cdot \\ \mathbf{N}_{,z} & \cdot & \cdot & \cdot \\ \cdot & \cdot & \cdot & \cdot \\ \cdot & \cdot & \cdot & \cdot \\ \cdot & \cdot & \cdot & \cdot \\ \cdot & \cdot & \cdot & -\mathbf{N}_{,z} \end{bmatrix}, \tag{A1}$$

where

$$\mathbf{N} = \begin{bmatrix} N_1 & \cdot & \cdot & \cdot & N_2 & \cdot & \cdot & \cdot & N_3 & \cdot & \cdot & \cdot \\ \cdot & N_1 & \cdot & \cdot & \cdot & N_2 & \cdot & \cdot & \cdot & N_3 & \cdot & \cdot \\ \cdot & \cdot & N_1 & \cdot & \cdot & \cdot & N_2 & \cdot & \cdot & \cdot & N_3 & \cdot \\ \cdot & \cdot & \cdot & N_1 & \cdot & \cdot & \cdot & N_2 & \cdot & \cdot & \cdot & N_3 \end{bmatrix}.$$

N_1, N_2 and N_3 are quadratic interpolation functions with three equally spaced nodal surfaces given as,

$$N_1 = \frac{1}{2}z(z-1), \quad N_2 = 1 - z^2, \quad \text{and } N_3 = \frac{1}{2}z(z+1), \quad \text{where } -1 \leqslant z \leqslant 1.$$

Eq. (5) can be expressed in terms of Eq. (3) as:

$$\begin{aligned} \mathrm{KE} &= \frac{1}{2}\int \dot{\mathbf{v}}^{e\mathrm{T}}\mathbf{m}^{e}\dot{\mathbf{v}}^{e}\,\mathrm{d}x, \\ H &= \frac{1}{2}\int (\mathbf{v}_{,x}^{e\mathrm{T}}\mathbf{k}_{11}\mathbf{v}_{,x}^{e} + \mathbf{v}_{,x}^{e\mathrm{T}}\mathbf{k}_{12}\mathbf{v}^{e} + \mathbf{v}^{e\mathrm{T}}\mathbf{k}_{21}\mathbf{v}_{,x}^{e} + \mathbf{v}^{e\mathrm{T}}\mathbf{k}_{22}\mathbf{v}^{e})\mathrm{d}x, \\ W &= \frac{1}{2}\int \mathbf{v}^{e\mathrm{T}}\mathbf{f}^{e}\,\mathrm{d}x, \end{aligned} \tag{A2}$$

where,

$$\mathbf{m}^{e} = \int \mathbf{N}^{\mathrm{T}}\boldsymbol{\rho}N\,\mathrm{d}z, \quad \mathbf{k}_{ij} = \int \mathbf{B}_{i}^{\mathrm{T}}\mathbf{C}\mathbf{B}_{j}\,\mathrm{d}z, \quad \text{and } \mathbf{f}^{e} = \int \mathbf{N}^{\mathrm{T}}\mathbf{f}\,\mathrm{d}z, \quad \text{for } i,j = 1,2,3.$$

Carrying out the variations on Eq. (4), the motion equation for a single element is obtained:

$$\mathbf{m}^{e}\ddot{\mathbf{v}}^{e} + \mathbf{k}_{1}^{e}\mathbf{v}^{e} + \mathbf{k}_{2}^{e}\mathbf{v}_{,x}^{e} - \mathbf{k}_{3}^{e}\mathbf{v}_{,xx}^{e} = \mathbf{f}^{e}, \tag{A3}$$

where

$$\mathbf{k}_{1}^{e} = \mathbf{k}_{22}, \quad \mathbf{k}_{2}^{e} = \mathbf{k}_{21} - \mathbf{k}_{12}, \quad \text{and } \mathbf{k}_{3}^{e} = \mathbf{k}_{22}.$$

References

Auld, B.A., 1990. Acoustic Fields and Waves in Solids, second ed. Krieger Publishing, Malabar, FL, USA.

Bai, H., Taciroglu, E., Dong, S.B., Shah, A.H., 2004. Elastodynamic green's functions for a laminated piezoelectric cylinder. International Journal of Solids and Structures 41, 6335–6350.

Bouakaz, A., Frigstad, S., Ten Cate, F.J., de Jong, N., 2002. Super harmonic imaging: a new imaging technique for improved contrast detection. Ultrasound in Medicine and Biology 28 (1), 59–68.

Chen, J., Chen, H., Pan, E., Heyliger, P.R., 2007. Modal analysis of magneto-electro-elastic plates using the state-vector approach. Journal of Sound and Vibration 304, 722–734.

Clorennec, D., Prada, C., Royer, D., 2007. Local and non-contact measurements of bulk acoustic wave velocities in thin isotropic plates and shells using zero group velocity Lamb modes. Journal of Applied Physics 101 (3), 034908-1–034908-6.

Datta, S.K., 2000. Wave propagation in composite plates and shells. In: Chou, T.W. (Ed.), Comprehensive Composite Materials, vol. 1. Elsevier, Amsterdam, pp. 511–558 (Chapter 1.18).

Dong, S.B., Pauley, K.E., 1978. Plane waves in anisotropic plates. Journal of the Engineering Mechanics Division 104, 801–817.

Frijlink, M.E., Goertz, D.E., van Der Steen, A.F.W., 2005. Reduction of stent artifacts using high-frequency harmonic ultrasound imaging. Ultrasound in Medicine and Biology 31 (10), 1335–1342.

Frijlink, M.E., Goertz, D.E., Vos, H.J., Tesselaar, E., Blacquiere, G., Gisolf, A., Krams, R., van Der Steen, A.F.W., 2006. Harmonic intravascular ultrasound imaging with dual-frequency catheter. Ultrasound in Medicine and Biology 32 (11), 1649–1654.

Gibson, A., Popovics, J.S., 2005. Lamb wave basis for impact-echo method analysis. Journal of Engineering Mechanics 131 (4), 438–443.

Goldberg, R.L., Smith, S.W., 1994. Multilayer piezoelectric ceramics for two-dimensional array transducers. IEEE Transactions on Ultrasonics Ferroelectrics and Frequency Control 41 (5), 761–771.

Holland, S.D., Chimenti, D.E., 2004. High contrast air-coupled acoustic imaging with zero group velocity Lamb modes. Ultrasonics 42, 957–960.

Hossack, J.A., Hayward, G., 1991. Finite-element analysis of 1–3 composite transducers. IEEE Transactions on Ultrasonics Ferroelectrics and Frequency Control 38 (6), 618–629.

Huang, C., Marmarelis, V.Z., Zhou, Q., Shung, K.K., 2005. An analytical model of multilayer ultrasonic transducers with an inversion layer. IEEE Transactions on Ultrasonics Ferroelectrics and Frequency Control 53 (3), 469–479.

Lerch, R., 1990. Simulation of piezoelectric devices by two- and three-dimensional finite elements. IEEE Transactions on Ultrasonics Ferroelectrics and Frequency Control 37 (2), 233–247.

McKeighen, R., 2001. Finite element simulation and modeling of 2-D arrays for 3-D ultrasonic imaging. IEEE Transactions on Ultrasonics Ferroelectrics and Frequency Control 48 (5), 1395–1405.

Mills, D.M., Smith, S.W., 2002a. Multi-layered PZT/polymer composites to increase signal-to-noise ratio and resolution for medical ultrasound transducers Part II: Thick film technology. IEEE Transactions on Ultrasonics Ferroelectrics and Frequency Control 49 (7), 1005–1014.

Mills, D.M., Smith, S.W., 2002b. Finite element comparison of single crystal vs. multi-layer composite arrays for medical ultrasound. IEEE Transactions on Ultrasonics Ferroelectrics and Frequency Control 49 (7), 1015–1020.

Mukdadi, O.M., Desai, Y.M., Datta, S.K., Shah, A.H., Niklasson, A.J., 2002. Elastic guided waves in a layered plate with rectangular cross section. Journal of the Acoustical Society of America 112 (5), 1766–1779.

Mukdadi, O.M., Datta, S.K., 2003. Transient ultrasonic guided waves in layered plates with rectangular cross section. Journal of Applied Physics 93 (11), 9360–9370.

Nakamura, K., Fukazawa, K., Yamada, K., Saito, S., 2003. Broadband ultrasonic transducers using a $LiNbO_3$ plate with a ferroelectric inversion layer. IEEE Transactions on Ultrasonics Ferroelectrics and Frequency Control 50 (11), 1558–1562.

Nakamura, K., Koyama, K., Odakura, S., Yamada, K., Saito, S., 2005. $LiNbO_3$ ultrasonic transducers with and inverted-domain layer for radiation to solid media. Japanese Journal of Applied Physics 44 (6B), 4482–4484.

Negishi, K., 1987. Existence of negative group velocities in Lamb waves. Japanese Journal of Applied Physics 26 (sup 26-1), 171–173.

Pauley, K.E., Dong, S.B., 1974. Analysis of plane waves in laminated piezoelectric plates. Wave Electronics 1, 265–285.

Ramirez, F., Heyliger, P.R., Pan, E., 2006. Free vibration response of two-dimensional magneto-electric-elastic laminated plates. Journal of Sound and Vibration 292, 626–644.

Saravanos, D.A., Heyliger, P.R., 1995. Coupled layerwise analysis of composite beams with embedded piezoelectric sensors and actuators. Journal of Intelligent Material Systems and Structures 6 (3), 350–363.

Saravanos, D.A., Heyliger, P.R., Hopkins, D.A., 1997. Layerwise mechanics and finite element for the dynamic analysis of piezoelectric composite plates. International Journal of Solids and Structures 34 (3), 359–378.

Siao, J.C-T., Dong, S.B., Song, J., 1994. Frequency spectra of laminated piezoelectric cylinders. ASME Journal of Vibration and Acoustics 16, 364–370.

Taciroglu, E., Liu, C.W., Dong, S.B., Chun, C.K., 2004. Analysis of laminated piezoelectric circular cylinders under axisymmetric mechanical and electrical loads with a semi-analytic finite element method. International Journal of Solids and Structures 41, 5185–5208.

Tiersten, H.F., 1969. Linear Piezoelectric Plates. Plenum Press, New York, USA.
Veidt, M., Liu, T.R., Kitipornchai, S., 2000. Experimental investigation of the acousto-ultrasonic transfer characteristics of adhesively bonded piezoceramic transducers. Smart Materials & Structures 9 (1), 19–23.
Wang, D.Y., Chan, H.L-W., 2003. A dual frequency ultrasonic transducer based on BNBT-6/epoxy 1–3 composite. Materials Science and Engineering B 99, 147–150.
Zhou, Q.F., Cannata, J., Shung, K.K., 2006. Design and modeling of inversion layer ultrasonic transducers using $LiNbO_3$ single crystal. Ultrasonics 44, 607–611.
Zhou, Q., Cannata, J.M., Guo, H., Huang, C., Marmarelis, V.Z., Shung, K.K., 2005. Half-thickness inversion layer high-frequency ultrasonic transducers using $LiNbO_3$ single crystal. IEEE Transactions on Ultrasonics Ferroelectrics and Frequency Control 52 (1), 127–133.